

Control of Compressible Shear-Layer Development Downstream of a Backward-Facing Step by Nanosecond-Pulsed Plasma Actuator

By Z.L. Chen, I. Bolgar[†], C.J. Kähler[†] AND N. A. Adams[‡]

School of Aeronautics, Northwestern Polytechnical University, Xi'an, Shaanxi, 710072, China

Compressible flow over a backward-facing step (BFS) is of rich flow physics and practical importance. The flow dynamics are proposed to be studied by using a large-eddy simulation (LES) method. As the free shear layer is receptive to the thermal forcing, a nanosecond-pulsed dielectric barrier discharge (NS-DBD) plasma actuator is adopted for control of the compressible flow over the BFS. The flow control effects of NS-DBD is modeled by a discharge model using drift-diffusion equations and simplified air chemistry coupled to the LES through the gas heating. The predicted mean base flow is compared reasonably well with the experimental results. The state of the incoming boundary layer is changed by the plasma actuation. The subsequent free-shear layer development is modified. Consequently, the reduced fluctuations of the velocity, pressure and density were obtained in the recirculation region.

1. Introduction

Flow over a backward-facing step (BFS) is enriched by the fixed separation of the upstream boundary layer. It is of fundamental and practical importance due to its ingredients of multiple flow elements and presence in applied aerodynamics. The complex flow phenomenon has components of attached incoming boundary layer, fixed separation, free-shear layer, recirculation and reattachment. If the incoming flow is supersonic, there can be much more complex phenomenon [1], including sudden expansion, lip shock, reattachment compression and reattachment shock. Among many applications, the backward facing step is often used for ignition and flame holding in a scramjet engine and is a structural feature before a rocket nozzle [6].

Since the pioneering experimental study of Eaton and Johnston [4] there has been considerable amount of researches on BFS flows, including numerous computational studies [5]. Due to the progress of experimental techniques including high-speed Particle Image Velocimetry (PIV) and nanoparticle based planar laser scattering (NPLS), and advancement of computational power, interests in compressible flows over BFS relevant for fundamental understanding and in practical applications have grown most recently [3].

[†] Institute of Fluid Mechanics and Aerodynamics, Bundeswehr University Munich, 85577 Neubiberg, Germany

[‡] Lehrstuhl für Aerodynamik und Strömungsmechanik, Technische Universität München Boltzmannstr. 15, 85748 Garching b. München

For the complex supersonic flows over BFS, the numerical methods based on Reynolds-averaged Navier-Stokes (RANS) can just achieve favorable statistical results with data from experiments [2]. As is seen from a survey of the available literatures, interest in direct numerical simulation (DNS) and large-eddy simulation (LES) of the compressible separated shear flows in the practical applications has grown only recently [6]. Moreover, there has been only few studies of the backward-facing step configuration, none of which attempted to evaluate the role of compressibility.

Different passive and active flow control methods were used to reduce the large pressure fluctuations and additional pressure drag produced by the BFS. A permeable surface at reattachment region can passively reduce the peak root-mean-square (rms) pressure fluctuation up to 13% and drag of about 9% at low freestream speed [7]. Different shapes of the step edge were used to control the fully turbulent flow over BFS at Mach number 0.8 and 2.0 and the corresponding Reynolds numbers of $Re_h = 180,000$ and 210,000 [8].

Active flow control methods have the potential to control the flows over BFS without adverse effects at off-design conditions. Dielectric barrier discharge (DBD) plasma actuators driven by Alternating Current (AC) and nanosecond (NS) voltage pulse as active flow-control devices have been intensively investigated over last decade, because of their attractive advantages over the passive mechanical control devices, such as very short reaction time, without moving part, low weights and sizes, wideband control authority and low energy consumption [12].

Most recently NS-DBD plasma actuators have been numerically and experimentally investigated [10]. They are geometrically constructed as AC-DBD, having two asymmetrically distributed electrodes separated by a dielectric layer, but are driven by nanosecond high voltage pulses. They have been successfully applied for high-speed flow control, such as transonic leading-edge separation control on wings [11], the manipulation of bow shock ahead of a circular cylinder at Mach 5 [9] and transonic cavity noise reduction [13].

Based on our previous works on nanosecond pulsed discharge modeling [16] and on the high-speed flow controls using NS-DBD [14], we adopt NS-DBD to control the transonic and supersonic flow over the BFS. The objectives of the present proposal are (1) study the fundamental physics of flow over BFS at transonic and supersonic conditions corresponding to the experiments of Bolgar et. al. [3], including compressibility effects on the separated shear layer development, oscillations of the reattachment point and the pressure fluctuations; (2) figure out the capability and mechanism of NS-DBD plasma actuator to control the high-speed turbulent flow over the BFS, including the statistical and transient effects.

2. Numerical method

2.1. Fluid flow model

The unsteady compressible Navier-Stokes equations in conservative form are used to describe the flow dynamics, which are written as:

$$\partial_t \mathbf{U} + \nabla \cdot \mathbf{F}(\mathbf{U}) + \nabla \cdot \mathbf{D}(\mathbf{U}) = \mathbf{S}, \quad (2.1)$$

with the conservative variable vector $\mathbf{U} = [\rho, \rho u_1, \rho u_2, \rho u_3, E]^T$. The conserved variables are density ρ , momentum ρu_i and total energy $E = \rho e + 0.5 \rho u_i u_i$. The convective flux is

$$\mathbf{F}_i(\mathbf{U}) = [u_i \rho, u_i \rho u_1 + \delta_{i1} p, u_i \rho u_2 + \delta_{i2} p, u_i \rho u_3 + \delta_{i3} p, u_i (E + p)]^T,$$

and the diffusive flux is

$$\mathbf{D}_i(\mathbf{U}) = [0, -\tau_{i1}, -\tau_{i2}, -\tau_{i3}, -u_k\tau_{ik} + q_i]^T, \quad (2.2)$$

where u_i is the velocity vector, τ_{ij} are the components of the viscous stress tensor

$$\tau_{ij} = \mu(\partial_j u_i + \partial_i u_j - 2/3\delta_{ij}\partial_k u_k), \quad (2.3)$$

and the heat flux is

$$q_i = -\kappa\partial_i T. \quad (2.4)$$

The transport properties, dynamic viscosity μ and thermal conductivity κ depend on temperature T . They are calculated as

$$\mu = \mu_\infty \left(\frac{T}{T_\infty}\right)^{2/3}, \quad \kappa = \frac{\mu c_p}{Pr}, \quad (2.5)$$

where μ_∞ and T_∞ are the freestream dynamic viscosity and temperature. $c_p = \gamma R / (\gamma - 1)$ is the heat capacity at constant pressure with $\gamma = 1.4$ and gas constant $R = 287.15 (J/kg \cdot K)$. A constant Prandtl number $Pr = 0.72$ for air is used. To close the system of equations the pressure p and temperature T are related to density ρ and internal energy ρe by the equation of state

$$p = \rho RT = (\gamma - 1)\rho e. \quad (2.6)$$

The source term \mathbf{S} is taken as $[0, f_x, f_y, f_z, q_m + f_i u_i]^T$, where f_i and q_m are the electric force and power density of the gas discharge, respectively. The electric force is so small that can be neglected due to its weak effect according to the experimental and numerical results.

An implicit LES method using Adaptive Local Deconvolution Method (ALDM) is adopted to reconstruct the flow variables from the cell-averaged values at the cell interfaces for the convective flux calculation [15]. The diffusion terms are discretized by using second-order central scheme. An explicit third order TVD Range-Kutta method is used for time advancing.

2.2. Gas discharge model

The discharge is modeled by the three-equation drift-diffusion fluid model, which contains the mass-conservation equations, an energy-conservation equation for the electrons and Poisson's equation for the pulse. The mass and energy conservation equations of the electrons are

$$\frac{\partial}{\partial t}(n_e) + \nabla \cdot \vec{\Gamma}_e = R_e, \quad (2.7)$$

$$\frac{\partial}{\partial t}(n_\varepsilon) + \nabla \cdot \vec{\Gamma}_\varepsilon + \vec{E} \cdot \vec{\Gamma}_e = R_\varepsilon, \quad (2.8)$$

where the subscripts e and ε indicate electron and electron energy, respectively. n_e and n_ε are the electron-number density and the electron-energy density. R_e and R_ε are the sources of the electrons and the electron energy due to chemical reactions. $\vec{\Gamma}_e$ and $\vec{\Gamma}_\varepsilon$ are the fluxes of the electron and the electron energy, which are

$$\vec{\Gamma}_e = -(\vec{\mu}_e \cdot \vec{E})n_e - \nabla(\vec{D}_e n_e) + n_e \vec{v}_c, \quad (2.9)$$

$$\vec{\Gamma}_\varepsilon = -(\vec{\mu}_\varepsilon \cdot \vec{E})n_\varepsilon - \nabla(\vec{D}_\varepsilon n_\varepsilon) + n_\varepsilon \vec{v}_c, \quad (2.10)$$

in the drift-diffusion approximation. $\vec{\mu}_e$, $\vec{\mu}_\varepsilon$, \vec{D}_e and \vec{D}_ε are the drift and diffusion coefficients of the electron and the electron energy, and they are calculated by the electron

energy probability function [16]. \vec{v}_c is the gas velocity. The source terms R_e and R_ε are $\sum \left((\alpha - \eta) \left| \vec{\Gamma}_e \right| + k_r \Pi n_r \right)$ and $\sum \left((\alpha - \eta) \left| \vec{\Gamma}_\varepsilon \right| \Delta\varepsilon + k_r \Delta r \Pi n_r \right)$,

where α is the ionization coefficient and η is the attachment coefficient. k_r is the reaction rate and n_r is the number density of the reactants. $\Delta\varepsilon$ and Δr are the energy loss of electronic ionization reactions and other electron impact reactions.

The mass-conservation equations of the heavy species are

$$\rho \frac{\partial}{\partial t} (\omega_k) = \nabla \cdot \vec{\Gamma}_k + R_k, \quad (2.11)$$

where ω_k is the mass fraction of the k heavy species. R_k is the source term of the species k due to the chemical reactions. $\vec{\Gamma}_k$ are the drift-diffusion approximation fluxes

$$\vec{\Gamma}_k = \rho \omega_k \left(D_k \frac{\nabla \omega_k}{\omega_k} + D_k \frac{\nabla M}{M} - z_k \mu_k \vec{E} \right) + \rho (\omega_k \vec{v}_c), \quad (2.12)$$

where μ_k and D_k denote the drift and diffusion coefficients of the k heavy species, respectively. The drift coefficients of ions are the functions of the reduced electric field [17]. The diffusion coefficients of ions and neutrals are calculated from the generalized Einstein relation and the classical gas kinetic theory [18], respectively. z_k is the charge number. M is the average molar mass. ρ is calculated by the equation of state for perfect gas as

$$\rho = \frac{pM}{RT}. \quad (2.13)$$

The electric potential ϕ induced by the space net charge is governed by the Poisson's equation

$$-\nabla \cdot (\varepsilon \nabla \phi) = e \sum (-n_e + z_k n_k), \quad (2.14)$$

where e is the elementary charge and ε is the permittivity. n_k are the number densities of the heavy species and $n_k = \omega_k N_A \rho / M_k$, where N_A is the Avogadro constant. Electric field is calculated from the potential as $\vec{E} = -\nabla \phi$.

The discharge energy is determined by the currents of the electrons, ions and the intensity of the electric field. It can be calculated as

$$Q_{D_ei} = \int_0^{T_p} P_{D_ei} dt = \int_0^{T_p} (P_{D_e} + P_{D_i}) dt = \int_0^{T_p} (\vec{J}_e \cdot \vec{E} + \vec{J}_i \cdot \vec{E}) dt = Q_{D_e} + Q_{D_i}, \quad (2.15)$$

where T_p is the integrating time. The subscripts D_ei , D_e and D_i denote the discharge energy, the electrons' energy and the ions' energy.

The gas heating is composed of the energy of electron elastic-collision and rotational excitation ($el - r$), the electron energy spent in electronic excitation (E) [19], the energy stored in the vibrational excitation (V) and the ions' energy. The details are given in the previous paper [16].

The gas heating (GH) can be predicted as

$$Q_{GH} = \int_0^{T_p} (P_{GH}) dt = \int_0^{T_p} (P_{D_i} + P_{el-r} + P_E + P_{VT}) dt, \quad (2.16)$$

In order to reduce the computational cost, the fluid model and the gas discharge model are not fully coupled. The mean-flow pressure, density, temperature and velocity from the flow are used and are kept constant during the gas discharge. The mean power

Ma_∞	U_∞	δ_{99}/h	H_{12}	Re_{δ_2}	Re_h
0.80	258	0.35	1.39	7400	180,000
2.00	511	0.47	1.49	7900	208,000

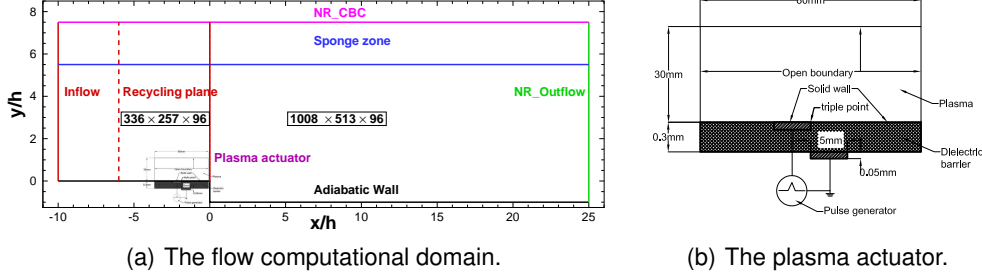
TABLE 1. Incoming boundary parameters of the simulation cases at $x/h = -1.0$ [3].

FIGURE 1. The computational domains and the plasma actuator.

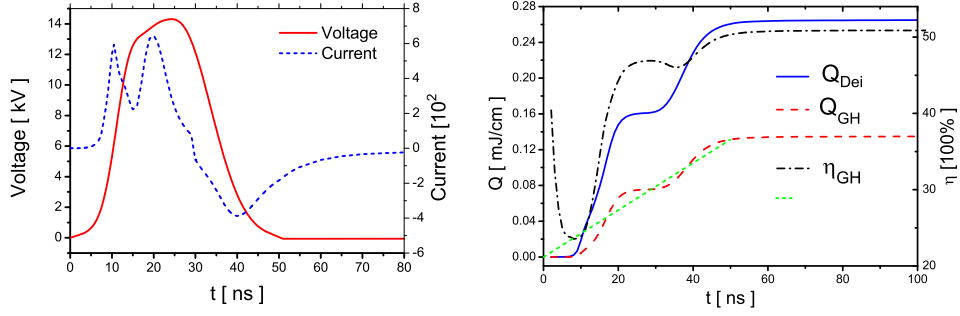
density $q_m = Q_{GH}/T_p$ from the gas discharge model is loosely coupled to the Navier-Stokes equation as a energy source term, as given in Eq. 2.1.

The governing equations (2.7), (2.8), (2.11) and (2.14) are solved by using a finite element method [16, 20]. A second-order Lagrange shape function is used for each element.

2.3. Simulation setup

The same step as in the experiments of Bolgar et al. [3] is adopted in the numerical simulation. In the flow flow simulation, the computational domain which is non-dimensionalized by the step height h , is shown in Fig. 1(a). The curved leading edge upstream of the step is not included. The spanwise width is $2h$. A recycling inflow boundary condition is applied at the inlet with the recycling plane of $6h$ downstream. Non-reflective characteristic boundary conditions are applied at outlet and upper boundary. A sponge zone from $y/h = 5.5$ to $y/h = 7.5$ is applied to weaken the wave reflection of the upper boundary. The periodic boundary condition is applied in the spanwise direction. The no-slip adiabatic wall is applied on all other boundaries. The flow field is initialized using boundary-layer velocity profiles based on the wall distance and the measured boundary layer thickness at $x/h = -1$ of the experiment, as summarised in Table 1. The grid resolution upstream of the step is $336 \times 257 \times 96$ in the streamwise, wall-normal and spanwise direction, respectively. The grid resolution downstream of the step is $1008 \times 513 \times 96$. The grids are refined near the step and the wall in the streamwise and wall-normal direction, respectively. In the spanwise direction, the grid is uniformly distributed.

In the gas discharge simulation, the computational domain is also shown in Fig. 1(b). The plasma actuator is also shown in detail. In the flow control cases, the plasma actuator is flush mounted on the wall upstream the step. The right tip of the exposed electrical electrode lies at $x/h = -1.0$. The number of the computational nodes is 1,207,356 and the corresponding number of elements is 2,379,428. The initial and boundary conditions and the adaptive time steps are the same as in our previous work [16].



(a) Voltage and current of the gas discharge. (b) Discharge energy, gas heating and gas-heating efficiency.

FIGURE 2. The voltage, current and energy characteristics of the gas discharge.

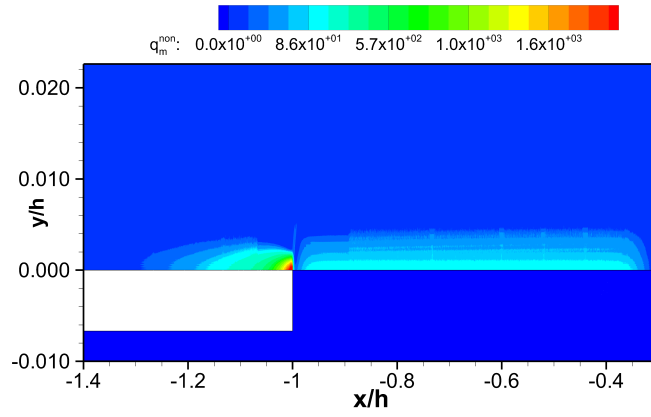


FIGURE 3. The distribution of the non-dimensional mean power density of the gas heating.

3. Results and discussions

3.1. Gas discharge

The mean flow field from the flow simulation is used as the discharge environment in the gas discharge simulation. As the plasma sheath is quite thinner than the boundary layer, the effect of the velocity on the discharge is weak [16]. However, the effects of the gas pressure, density and temperature on the gas discharge are strong, which can be well scaled using scaling law [16].

The applied voltage and the resultant current are shown in Fig. 2(a) at free-stream Mach number 0.8. The total discharge energy Q_{Dei} , the gas heating Q_{GH} and the consequent gas-heating efficiency ($\eta_{GH} = Q_{GH}/Q_{Dei}$) are shown in Fig. 2(b). The gas-heating efficiency at the end of the pulse is 51%, which is correlated well with the experimental results. The instantaneous gas-heating magnitude changes according to the applied voltage. At the voltage rising and falling stages, the gas-heating effects are strong. However, in the plateau stage the gas-heating effect is quite weak. The linearized gas heating is also shown in Fig. 2(b), which follows the profile of the gas heating well. During the gas discharge under a short pulse of 50 ns, the linearization of the gas heating is reasonable for the flow simulation.

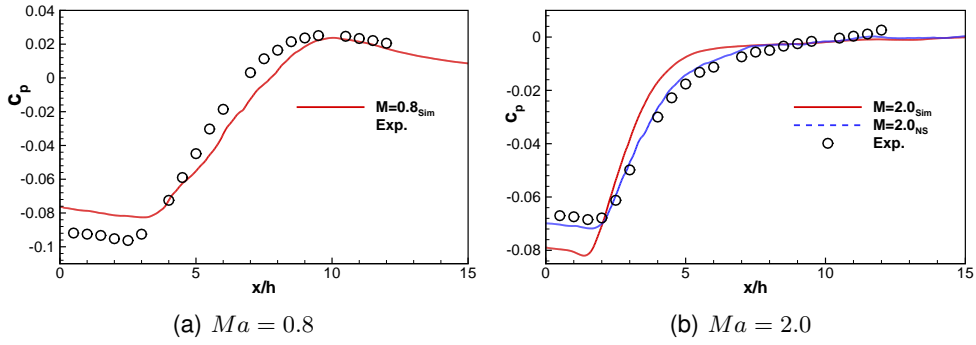


FIGURE 4. The comparisons of the mean pressure coefficients downstream of the step at $Ma = 0.8$ and $Ma = 2.0$.

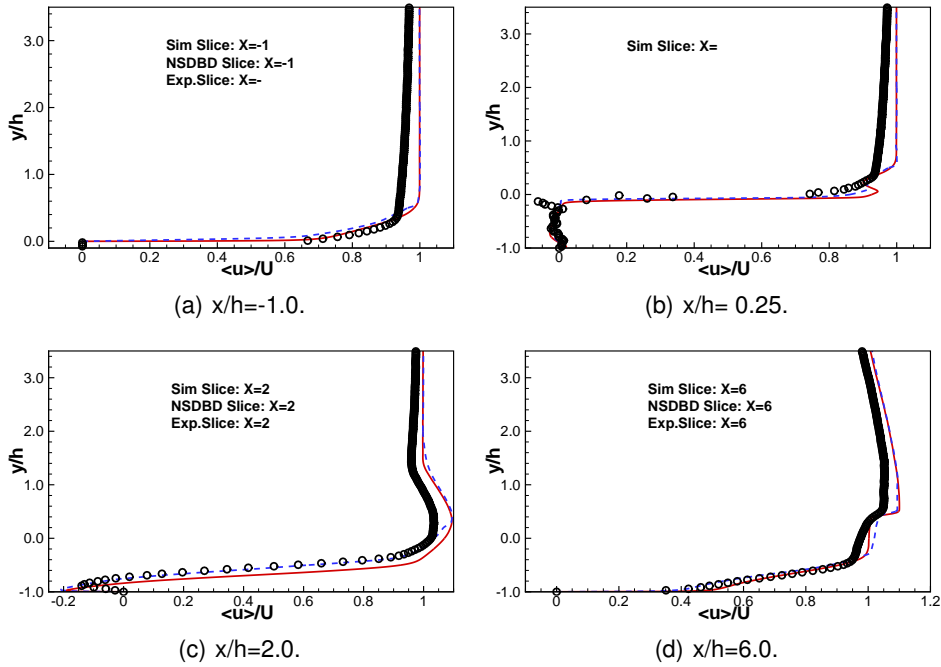


FIGURE 5. The comparisons of the mean streamwise velocity at different streamwise position $X = x/h$ at $Ma = 2.0$.

The distribution of the non-dimensional mean power density $q_m^{non} = q_m h / (\rho_\infty U_\infty^3)$ is shown in Fig. 3. The maximum magnitude reaches up to 1600 at the right tip of the exposed electrode, where a cylinder compression wave can be promoted in the flow field. It also leads to computational difficulty on the limitation of the time step in the flow simulation.

3.2. Flow field without and with control

In this section the pressure coefficient, mean flow velocity and Reynolds shear stress are compared with the experimental results of Bolgar et. al. [3]. Then the effects of the plasma actuation are analyzed.

3.2.1. Mean flow field of the base flow

The pressure coefficients defined as $c_p = (p - p_\infty)/p_{tot}$ are compared with the experimental results on the wall after the step at $Ma = 0.8$ and $Ma = 2.0$, as shown in Fig. 4(a) and Fig. 4(b), respectively. p_∞ is the free-stream static pressure and p_{tot} is the free-stream total pressure. Due to the time-step limitation and computational cost at the transonic condition, the simulation is not well converged at $Ma = 0.8$, as shown in Fig. 4(a). Therefore, the following analysis mainly focuses on the supersonic case. The pressure coefficient is under predicted in the recirculation region, but is over predicted in the reattachment region. The pressure recovery is faster in the simulation than that in the experiment. This discrepancy may be caused by the state of the incoming boundary layer upstream of the step.

The mean streamwise velocity is compared with the experimental PIV results at different streamwise positions. Upstream of the step the predicted boundary layer is thicker than that in the experiment. The streamwise velocity exhibiting a wall-normal gradient far away from the wall can be observed in the experiment. However, it reaches the free-stream velocity at the edge of the boundary layer in the simulation. Just downstream of the step it has a velocity defect in the separated free shear layer in the simulation. A fast flow region is observed at $x/h = 1.0$ due to the flow expansion after the step. The recirculation is stronger than that in the experiment, which is consistent with the under-predicted pressure shown in Fig. 4(b). The expansion is stronger than that in the experiment, as shown in Fig. 5(c). The mean reattachment point is at $x/h = 2.7$, which is comparable with the experimental result. After the reattachment the velocity is predicted well near the wall, as shown in Figs. 5(d). And the position of the recompression shock is also predicted well.

The comparisons of the mean vertical velocity are given in Fig. 6 at the same streamwise positions as in the Fig. 5. Upstream of the step the predicted vertical velocity is positive, which means the flow moves away from the wall. However, it is negative in the experiment, which is quite different with that of the boundary layer over the flat plate. Downstream of the step the mean vertical velocity is predicted well away from the wall and the free shear layer. In the free-shear layer it is over predicted. Near the wall this also shows some discrepancies between the simulation and the experiment.

The Reynolds stresses of simulation and experiment are compared in Fig. 7. Upstream of the step the predicted results indicate that the incoming boundary layer develops well into the fully turbulent. The experimental results are not smooth due to the laser light sheet reflections in the PIV. Downstream of the step the Reynolds shear stress is predicted well away from the free-shear layer.

From the comparisons of the mean flow field it can be concluded that the mean flow is predicted reasonably well compared with the experimental result. The discrepancies could be mainly related to the state of the incoming boundary layer.

3.2.2. The effects of the plasma actuation

When the plasma actuation is applied the mean velocity and Reynolds shear stress are compared with that of the base flow in Figs. 5, 6 and 7. Ahead of the step the mean streamwise velocity changes very small near the wall. Away from the boundary layer, the velocity is identical in both cases with and without control, as shown in Figs. 5(a). However, the actuation introduces large vertical velocity near the wall, as shown in Figs. 6(a). After the step the mean streamwise and vertical velocities are almost the same away from the free-shear layer. However, there is obvious difference in

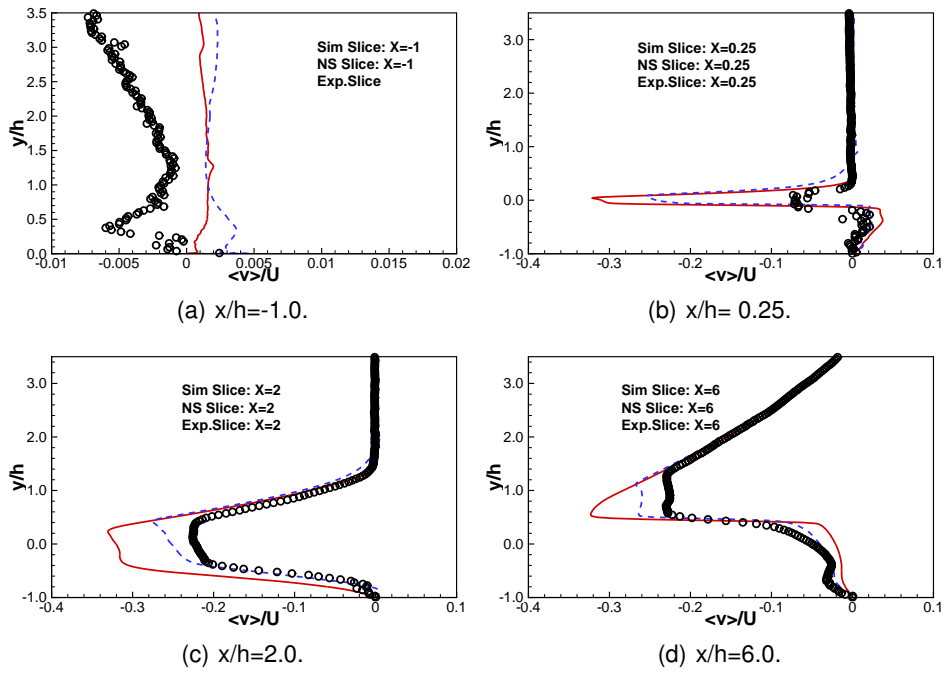


FIGURE 6. The comparisons of the mean vertical velocity at different streamwise position $X = x/h$ at $Ma = 2.0$.

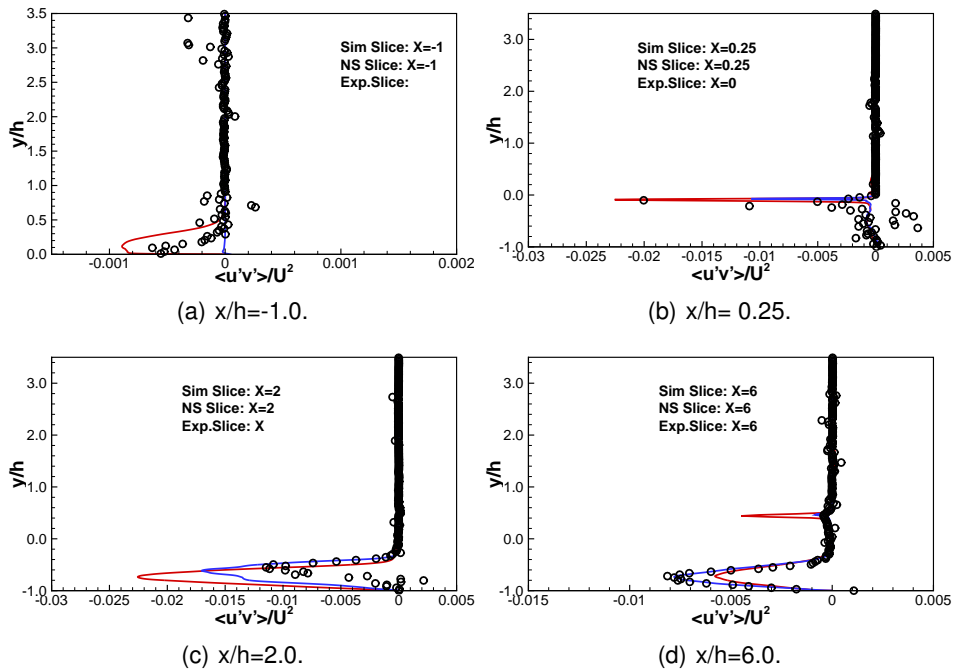


FIGURE 7. The comparisons of the Reynolds shear stress at different streamwise position $X = x/h$ at $Ma = 2.0$.

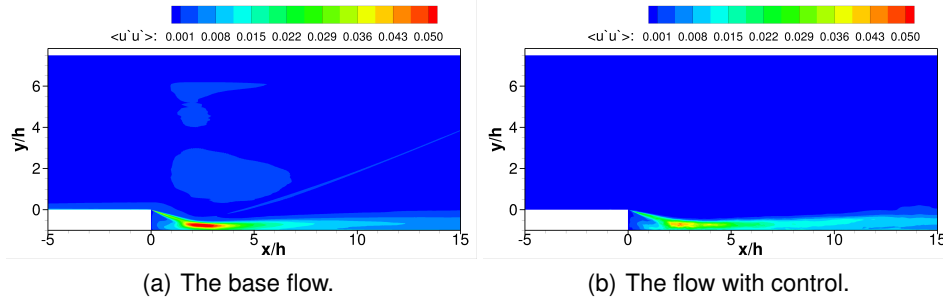


FIGURE 8. The comparisons of the Reynolds normal stresses without and with control at $Ma = 2.0$.

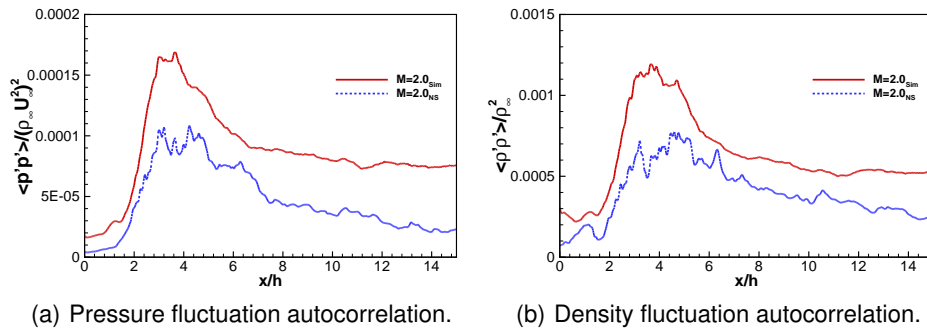


FIGURE 9. The comparisons of pressure and density fluctuations with and without control.

the recirculation region and the length of the recirculation is enlarged to $x/h = 3.2$ by the plasma actuation. Downstream of the reattachment the difference becomes small. One obvious change of the Reynolds shear stress occurs upstream of the step, as shown in Figs. 7(a), where the Reynolds shear stress is almost zero in the gas-discharge region. Therefore, the state of the incoming boundary layer changes. Downstream of the step the Reynolds shear stress decreases due to the control. Away from the free-shear layer it is almost the same with that without control. At $x/h = 4$ the Reynolds shear stress is almost the same in the shear layer in both cases. At $x/h = 6$ and $x/h = 8$ the Reynolds shear stress in the base case is smaller than that in the controlled case. However, it is obvious that the Reynolds shear stress decreases in the recompression region with the plasma actuation.

The Reynolds normal stresses are compared in Fig. 8. The magnitudes of the maximum stresses are reduced by plasma actuation. Additionally, the mean pressure and density fluctuations on the wall are compared in Fig. 9. Both strength of the fluctuations are reduced by the plasma actuation.

From the comparisons it can be seen that the controlled flow is better correlated to the experimental results. Therefore, it is suspected that the incoming boundary layer in the experiment is not fully developed. To exhibit the states of the incoming boundary layer the instantaneous computational Schlieren image is compared in Figs. 10. The state change of the incoming boundary layer is confirmed. Each plasma actuation promotes a compression wave as shown in Fig. 10(b) and a spanwise coherent structure.

From the analysis it can be concluded that the plasma actuation changes the devel-

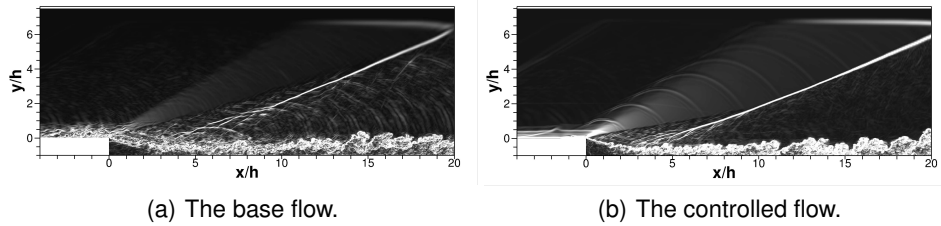


FIGURE 10. The comparisons of the numerical Schlieren image of the flow with and without control.

opment of separated shear layer by changing the state of the incoming boundary layer. The reduction of the velocity, pressure and density fluctuations are observed.

4. Conclusions

The supersonic flow over a backward-facing step was controlled by using nanosecond DBD plasma actuator. An implicit LES model using ALDM was adopted to simulate the fluid flow. A three-equation drift-diffusion model with a 4-species 4-reaction air chemistry was used to predict the gas discharge. Both models were loosely coupled by the gas-heating from the plasma model to the LES. From the gas discharge a very strong gas heating effect was obtained during the discharge. The predicted mean base flow was compared reasonably well with the experimental results. The reduced fluctuations of the velocity, pressure and density were obtained in the recirculation region by applying the plasma actuation through the changing of the state of the incoming boundary layer and the consequent free-shear layer development.

Acknowledgments

Financial support has been provided by the German Research Foundation (Deutsche Forschungsgemeinschaft – DFG) in the framework of the Sonderforschungsbereich Transregio 40 and National Natural Science Foundation of China under contract No. 11402211. Computational resources were provided by the High Performance Computing Center of Tianjin, China.

References

- [1] SMITH, H.E. (1967). The flow field and heat transfer downstream of a rearward facing step in supersonic flow. *Aerospace Research Laboratories*, (67-0065).
- [2] HERMANN, F.F., DOMINIC, A.V. AND RICHARD, D.S. (2006). A methodology for simulating compressible turbulent flows. *Journal of Applied Mechanics*, **73**, 405–412.
- [3] BOLGAR, I., SCHARNOWSKI, S. AND KÄHLER, C.J. (2018). The effect of the mach number on a turbulent backward-facing step flow. *Flow Turbulence Combust*, **101**(3), 653–680.
- [4] EATON, J.K. AND JOHNSTON, J.P. (1980). Turbulent flow reattachment: A experimental study of the flow structure behind a backward facing step. *Report, Thermosciences Division, Dept. Mechanical Engineering, Stanford University*, MD–39.

- [5] SENGUPTA, K., ZHANG, K.K.Q. AND MASHAYEK, F. (2009). Direct numerical simulation of compressible flow over a backward-facing step. CiteSeerX. DOI 10.1.1.528.1355.
- [6] BENEDDINE, S., BODERE, E. AND SIPP, D. (2015). Stability analysis of a compressible turbulent flow over a backward-facing step. *15th European Turbulence Conference*, 251–273.
- [7] HEENAN, A. AND MORRISON, J. (1998). Passive control of pressure fluctuations generated by separated flow. *AIAA Journal*, **36**(6), 1014–1022.
- [8] BOLGAR, I., SCHARNOWSKI, S. AND KÄHLER, C.J. (2019). Passive flow control for reduced load dynamics aft of a backward-facing step. *AIAA Journal*, **57**(1), 120–131.
- [9] NISHIHARA, M., TAKASHIMA, K., RICH, J. AND ADAMOVICH, I. (2011). Mach 5 bow shock control by a nanosecond pulse surface dielectric barrier discharge. *Phys. Fluids*, **23**, 066101.
- [10] ADAMOVICH, I., LITTLE, J., NISHIHARA, M., TAKASHIMA, K. AND SAMIMY, M. (2012). Nanosecond pulse surface discharges for high-speed flow control. *AIAA paper*, 2012–3137.
- [11] ROUPASSOV, D., NIKIPELOV, A., NUDNOVA, M. AND STARIKOVSKII, A.Y. (2009). Flow separation control by plasma actuator with nanosecond pulsed-periodic discharge. *AIAA J.*, **47**(1), 168–185.
- [12] WANG, J., CHOI, K., FENG, L., JUKES, T. AND WHALLEY, R. (2013). Recent developments in dbd plasmaflow control. *Prog. Aerosp. Sci.*, **62**, 52–78.
- [13] CHEN, Z., ZHANG, B., HICKEL, S. AND ADAMS, N. (2015). Implicit les of noise reduction for a compressible deep cavity using pulsed nanosecond plasma actuator. *ERCRAFTAC Workshop Direct and Large-Eddy Simulation IX (DLES9)*, 327–334.
- [14] CHEN, Z., ZHANG, B., HICKEL, S. AND ADAMS, N. (2015). Spatially developing laminar mixing layer forced by velocity and thermal perturbations downstream of a splitter plate. In: *9th International Symposium on Turbulence and Shear Flow Phenomena*. Melbourne, Australia.
- [15] HICKEL, S., EGERER, C. AND LARSSON, J. (2014). Subgrid-scale modeling for implicit large eddy simulation of compressible flows and shock-turbulence interaction. *Phys. Fluids*, **26**, 106101.
- [16] ZHANG, S., CHEN, Z., ZHANG, B. AND CHEN, Y. (2019). Numerical investigation on the effects of discharge conditions on a nanosecond pulsed surface dielectric barrier discharge. *Journal of Applied Physics*, **125**(11), 113301.
- [17] LAGMICH, Y., CALLEGARI, T., PITCHFORD, L.C. AND BOEUF, J.P. (2008). Model description of surface dielectric barrier discharges for flow control. *Journal of Physics D: Applied Physics*, **41**(9), 095205.
- [18] KEE, R.J., DIXON-LEWIS, G., WARNATZ, J., COLTRIN, M.E. AND MILLER, J.A. (1986). A fortran computer code package for the evaluation of gas phase multi-component transport properties. *Sandia Rep. SAND86-8246*.
- [19] BENILOV, M.S. AND NAIDIS, G.V. (2005). Modelling of discharges in a flow of preheated air. *Plasma Sources Science and Technology*, **14**(1), 129.
- [20] LIEBERMAN, M.A. AND LICHTENBERG, A.J. (2005). Principles of plasma discharges and materials processing, 2nd edition. *Principles of Plasma Discharges and Materials Processing*, **11**(78), 800.